

Topological superconductivity on the honeycomb lattice: Effect of normal state topology

Sebastian Wolf,¹ Tyler Gardener,¹ Karyn Le Hur,² and Stephan Rachel¹

¹*School of Physics, University of Melbourne, Parkville, VIC 3010, Australia*

²*CPHT, CNRS, Institut Polytechnique de Paris, Route de Saclay, 91128 Palaiseau, France*

The search for topological superconductors is one of the most pressing and challenging questions in condensed matter and material research. Despite some early suggestions that *doping a topological insulator* might be a successful recipe to find topological superconductors, until today there is no general understanding of the relationship of the topology of the superconductor and the topology of its underlying normal state system. One of the major obstacles is the strong effect of the Fermi surface and its subsequent pairing tendencies within the Hubbard model framework, usually preventing a detailed comparison between different topological superconducting systems. Here we present an analysis of doped insulators—topological and trivial—where the dominant Fermi surface effects have been equalized. Our approach allows us to study and compare superconducting instabilities of different normal state systems and present rigorous results about the influence of the normal state system's topology.

I. INTRODUCTION

Topological superconductors (TSCs)¹ are among the most desirable materials since their Majorana quasi particles exhibit Non-Abelian statistics² and are considered the prime candidates for topological quantum computing³. After searching for TSCs for a few decades, we still have not established a general method or a “recipe” of how to fabricate or synthesize them, despite some promising strategies^{4–9}. An exception constitute hybrid and engineered systems, where due to proximitization of *s* wave superconductivity the system's ground state can effectively become topologically non-trivial^{10–15}.

Here we focus on the key question what it takes to make unconventional superconductors – driven by electron correlations – topologically non-trivial. These *intrinsic* TSCs are often also referred to as spin-triplet or odd-parity superconductors. More generally, also gapped spin-singlet superconductors can be considered topologically non-trivial when they are chiral¹⁶, as *e.g.* realized through $d + id$ pairing on hexagonal lattices^{17–21}; chiral singlet pairing leads, however, to an even-valued Chern number and an even number of Majorana zero modes at defects, allowing them to annihilate into trivial states²². Examples of candidate materials for odd-parity pairing which have attracted much attention lately are UPt_3 ²³, CePt_3Si ^{24,25}, $\text{Cu}_x\text{Bi}_2\text{Se}_3$ ^{7,26,27}, $\text{Sn}_{1-x}\text{In}_x\text{Te}$ ^{28–30}, $\text{FeSe}_{0.45}\text{Te}_{0.55}$ ^{31–33} and UTe_2 ³⁴. Amongst them, $\text{Cu}_x\text{Bi}_2\text{Se}_3$ and $\text{Sn}_{1-x}\text{In}_x\text{Te}$ are of particular interest, since both their normal state systems represent doped topological materials: Bi_2Se_3 is a three-dimensional topological insulator (TI)³⁵ and SnTe a topological crystalline insulator³⁶. That raises the question whether it might be advantageous to search for TSCs in doped topological (insulating) materials. This central question has occurred since the discovery of TIs itself, since the Bloch matrix of TIs and the Bogoliubov–de Gennes matrix of TSCs can be form-equivalent. The simplest case to illustrate this, are the

two-orbital Chern insulator and the chiral *p* wave superconductor on the square lattice. Both two-dimensional matrices contain $\pm 2t[\cos(ap_x) + \cos(ap_y)]$ on the diagonal: $+$ ($-$) corresponds to the electron (hole) degree of freedom of the superconductor or to the single particle dispersions of the two different orbitals, respectively. The off-diagonal element is of the form $\sin(ap_x) + i\sin(ap_y)$ and realizes chiral $p_x + ip_y$ pairing, or the complex hybridization between the two orbitals responsible for the band inversion of the Chern insulator. Does this analogy imply that doped topological insulators possess an advantage in realizing topological superconductivity? An affirmative answer is not possible for two reasons: (i) (Topological) superconductivity emerges for energetic reasons, while topological states of matter such as TIs for symmetry reasons. (ii) TIs in their simplest form are non-interacting systems; in contrast, TSCs in the Bogoliubov–de Gennes framework are only treated on the mean-field level. Their full description requires, however, to include the electron–electron interactions of the many-body Hubbard model. As a consequence, it is *a priori* unknown what the pairing and the topology of the resulting superconducting groundstate might be. This situation calls for a systematic investigation of Hubbard models where the kinetic term can or cannot be topologically non-trivial. It is well-known, however, that already small changes of the Fermi surface (FS) can drastically influence which superconducting instability prevails; information about the topology of the normal state system is only stored in the eigenvectors of the Bloch matrix, due to the dominance of FS effects it is often difficult or even impossible to undertake such a systematic investigation.

In this Letter, we study the superconducting states of topologically different models on the honeycomb lattice. We carefully choose the system parameters such that their FSs are *identical*, thus equalizing the effect of the FS. The remaining main difference between these models, entering the calculation of the superconducting ground state, are their eigenvectors which store the in-

formation about the normal state system's topology. We apply the weak coupling renormalization group (WCRG) approach^{37–44} which limits us to infinitesimal repulsive interactions; however, the method is asymptotically exact.

II. MODELS AND METHODOLOGY

We study superconducting instabilities of four different bandstructures on the honeycomb lattice with additional Hubbard onsite interaction, realizing the simplest model to give an answer to the question of this Letter. Specifically, we consider as a topologically non-trivial system on the honeycomb lattice the Kane-Mele (KM) model^{45,46}, a time-reversal invariant \mathbb{Z}_2 TI. In addition, we study the inversion symmetry breaking Semenoff (Se) insulator⁴⁷, realized through a spin-independent staggered sublattice potential, and the antiferromagnetic Zeeman (AF) insulators⁴⁸, realized through an antiferromagnetic out-of plane Zeeman field as examples of topologically trivial insulators. These three models are complemented by the semi-metallic tight-binding model with nearest- and second-nearest neighbor hopping, referred to as graphene (Gr) in the following. The Hamiltonian is given by $\hat{H} = \hat{H}_0 + \hat{H}_{\text{int}}$ with

$$\begin{aligned} \hat{H}_0 &= \sum_{i,j} \sum_{s,s'} c_{is}^\dagger \hat{h}_{ij,ss'} c_{js'} , \\ \hat{H}_{\text{int}} &= U_0 \sum_i \sum_{s \neq s'} c_{is}^\dagger c_{is'}^\dagger c_{is'} c_{is} , \end{aligned} \quad (1)$$

where \hat{h} denotes the 4×4 hopping matrix, c_{is}^\dagger is the creation operator of an electron with spin s at site i , and U_0 is the onsite interaction strength. The Bloch matrix is defined for each of the four models in Sec. II of the Supplement⁴⁹; Fig. 1 contains a visual representation of all hopping and onsite terms. We note that the energy bands have the general form

$$E(\vec{k}, n) = \Lambda_0(\vec{k}) + n \sqrt{T_1^2(\vec{k}) + T_2^2(\vec{k}) + \Lambda_1^2(\vec{k})}$$

with the band index $n = \pm 1$. For simplicity the details of the \vec{k} dependent functions Λ_0 , T_1 , T_2 , and Λ_1 are shown in Sec. III of the Supplement⁴⁹. We stress that Λ_0 is non-zero only for the Gr model; for all other models the energy bands exhibit a particle-hole symmetry and it is sufficient to focus w.l.o.g. on the electron-doped case (*i.e.*, filling $n > 1$).

In the following, we emphasize some basic facts about superconductivity and the specific aspects on methodology which are key for this work.

While conventional, phonon-mediated superconductors form Cooper pairs with zero angular momentum (s wave), unconventional superconductors usually involve higher-angular momentum pairing channels (such as p , d , f wave). It is well-established that the crystal space group of the normal state dictates the possible irreducible

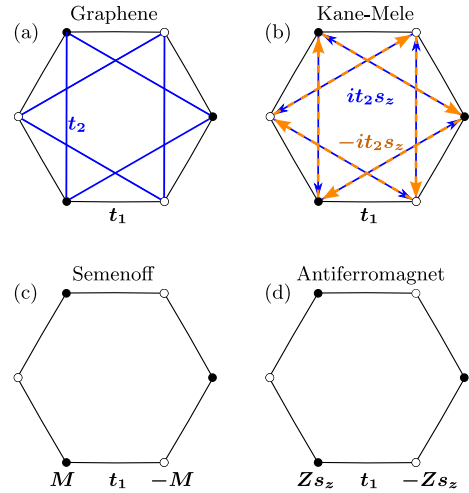


FIG. 1. Hoppings and onsite potentials of the four honeycomb lattice systems studied in this paper. Atoms on sublattice A (B) are indicated by full (empty) circles. a) Graphene model with nearest and next-nearest neighbor hoppings. b) Kane-Mele model, where the next-nearest neighbor hopping is imaginary, with opposite sign for clockwise (orange) and counter-clockwise (blue) hopping; in addition, there is a sign change for different spins. c) Semenoff model with staggered onsite potential M . d) Antiferromagnetic Zeeman model, which is similar to Semenoff model with the difference that the onsite potential Z changes sign for different spins.

representations (irreps), and the superconducting order parameter must transform according to one of these irreps⁵⁰. The symmetry analysis of the four considered models is summarized in Tab. I. Gr and KM correspond to symmetry group D_6 and Se and AF to D_3 . We note that the differences are small: D_3 only consists of the three irreps A , B and E , while they are split for D_6 into A_1 and A_2 , B_1 and B_2 as well as E_1 and E_2 . Most notably are the two-dimensional irreps E_1 containing the p wave and E_2 the d wave order parameters, which can form chiral superpositions such as $p_x + ip_y$ and $d_{xy} + id_{x^2-y^2}$. For D_3 these belong to the same irrep and could possibly be combined (which we have not observed here). We further note that the AF and KM models further break the $SU(2)$ spin rotation symmetry down to only $U(1)$ symmetry (*i.e.*, spin is still a good quantum number) which can lead to a splitting of the

TABLE I. Symmetries of the Bloch matrix of the four different models. TR denotes time reversal symmetry, I denotes inversion symmetry, C_n are rotations and M_i reflections.

Model	TR I		lattice symmetries					residual group
			C_2	C_3	C_6	M_x	M_y	
Gr	X	X	X	X	X	X	X	D_6
KM	X	X	X	X	X	X	X	D_6
Se	X			X			X	D_3
AF				X		X		D_3

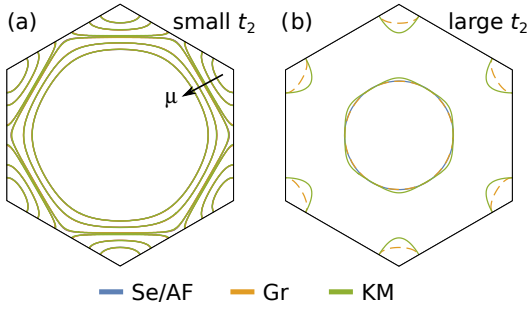


FIG. 2. (a) Fermi surfaces of the different models for small values of t_2 and different values of μ . We note that t_2 refers here either to the second neighbor hopping or to the onsite terms, respectively. For clarity, we only show a subset of all used values of μ : The six FSs closest to the corners of the BZ correspond to $\mu = 0.6$, and the almost circular FS in the center of the BZ to $\mu = 1.4$. The specific values of t_2 are listed in the Supplement for all values of μ ⁴⁹. (b) Fermi surfaces of the different models for large values of t_2 . We only show an example of Fermi surfaces which consist of multiple pockets, one in the center and additional ones in the corner of the BZ (KM and Gr models). Se and AF models only possess a single circular FS.

three degenerate triplet states into $S^z = 0$ and ± 1 components.

Superconductivity is a weak-coupling instability of the Fermi sea, thus small changes of single-particle parameters, which lead to changes of the FS, can have drastic effects on the symmetry of the superconducting ground state. In particular, small changes of the FS can trigger a phase transition between superconducting ground states which transform according to different irreps. We note that the applied WCRG is particularly sensitive to changes in the FS due to the vanishingly small interaction scale; we stress, however, that the same is true for other methods designed to work at intermediate coupling strength such as random phase approximation⁵¹ or functional renormalization group⁵². That is why it does not only make little sense to compare topological bandstructures on different lattice geometries, but neither is it very meaningful to compare them when their FSs are different. The honeycomb lattice with its low-energy Dirac bands offers the perfect setting to overcome both obstacles. Small-gap insulating phases are usually well characterized by a gapped Dirac Hamiltonian as an effective low-energy theory at both valleys of the honeycomb lattice. To lowest order, the gap term $\propto G$ is \vec{k} independent, $H_{\text{Dirac}} \sim k_x \sigma^x + k_y \sigma^y + G \sigma^z$. Thus it is clear that for small gap opening $\sim G$ and not too large doping, different insulating honeycomb lattice bandstructures can produce identical FSs. We show in Fig. 2 (a) that even for large electron doping FSs remain identical if parameters are carefully chosen. Moreover, we are able to adjust the second neighbor hopping t_2 and the filling n of the Gr model to match these FSs as well [see Fig. 2 (a)].

As a method we employ the WCRG which is a real-

ization of Kohn-Luttinger superconductivity⁵³. Details about the WCRG are delegated to the Supplement⁴⁹ (see, also, references^{54,55} therein). Here we only discuss the structure of the analytical expression of the two-particle vertex Γ which is the central object we compute. In second order of the local electron-electron interaction U_0 we have $\Gamma^{(2)} = \frac{1}{2}\Gamma_{\text{BCS}} + \Gamma_{\text{ZS}} + \Gamma_{\text{ZS}'}.$ The first contribution is referred to as the BCS diagram and the other two contributions as zero sound (ZS) diagrams⁵⁶. The BCS diagram diverges logarithmically, which indicates a phase transition, *i.e.*, that the normal state becomes unstable towards the superconducting state (superconductivity is the only instability in the weak coupling regime⁵³). The divergency is treated by renormalization, upon which we obtain the superconducting order parameter from the eigenvalue problem of the remaining two contributions Γ_{ZS} and $\Gamma_{\text{ZS}'}$. They take the form

$$\Gamma_{\text{ZS}}(2\bar{2}'\bar{1}'1) = \sum_{\vec{k}_3} \sum_{n_3 n_4} \sum_{\bar{s}_3 \bar{s}_4} M(\bar{2}'431)M(234\bar{1}') \times \frac{f(E(3)) - f(E(4))}{E(3) - E(4)}, \quad (2)$$

with the Fermi distribution $f(E)$. We use the short notation $1 \equiv \vec{k}_1, n_1, \bar{s}_1$, $\bar{1} \equiv -\vec{k}_1, n_1, \bar{s}_1$, $1' \equiv \vec{k}_1, n_1, \bar{s}_1'$. The expression (2) has essentially three ingredients: (i) The FS enters via incoming and outgoing momenta, \vec{k}_1 and \vec{k}_2 , respectively, and has a strong influence on the value of (2), as mentioned before. (ii) At zero temperature, the Lindhard function (the expression in the second line) contains the energy bands, albeit suppressed with $1/E$. In particular, here also energy states enter which are not at the FS. We have compared the energy bands of all four models, and the differences between them are very small or negligible; obviously they are biggest where Gr is gapless while all other models are gapped. Nonetheless, we expect the Lindhard expression to be essentially the same for all models, when their FSs are identical (see Sec. VI in⁴⁹). (iii) The third ingredient is the product of M factors which contain the eigenvectors \vec{v} of the Bloch matrix, containing the information about topology: $M(4321) = \sum_{l, s \neq s'} v_{l,s}^*(4) v_{l,s}(1) v_{l,s'}^*(3) v_{l,s'}(2) - \sum_{l, s \neq s'} v_{l,s}^*(4) v_{l,s}(2) v_{l,s'}^*(3) v_{l,s'}(1)$. The main idea of this paper is to prepare the four different models such that (i) and (ii) are essentially the same, and the remaining difference is (iii).

III. RESULTS

We choose $t_2 = 0.05t_1$ for the Kane-Mele model, leading to a relatively small gap of $3\sqrt{3}t_2 \approx 0.26t_1$ (in the following we refer to this as the “small gap” case); from an experimental perspective, this represents already a reasonable gap size. We adjust the Se and the AF models to have a comparable gap size and identical FSs; we also tune the Gr model to match the FS, although Gr

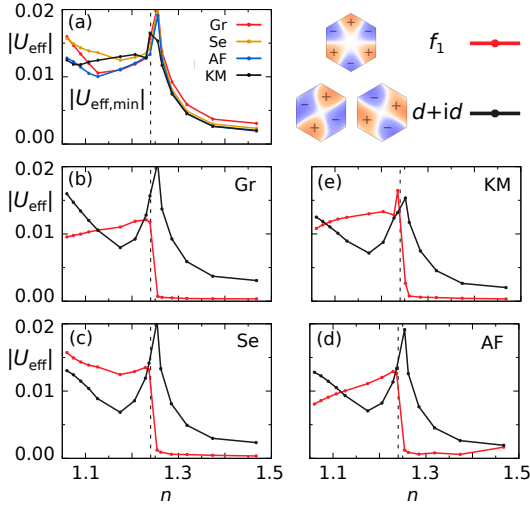


FIG. 3. Results for the systems corresponding to the “small gap” case, equivalent to $t_2 = 0.05t_1$ in the KM model. Filling and parameters of the other models are tuned to match the FSs of the KM model. Dashed lines indicate van Hove filling.

of course remains gapless. Note that we need to slightly adjust these parameters whenever we change the filling fraction in order to retain identical FSs (see Tab. S4 in the Supplement⁴⁹).

By virtue of WCRG we obtain the leading superconducting instabilities for the small gap case, shown in Fig. 3. Surprisingly, we find for all four models chiral $d + id$ wave pairing (E_2 irrep) to be dominating, when the filling is higher than van Hove filling (at $\mu/t_1 \approx 1$ corresponding to $n \approx 1.24$). Below van Hove filling, we find for all four models f wave pairing (B_1 irrep) as the leading instability, referred to as f_1 in the following. Only for even further reduced fillings, $d + id$ pairing wins once more (with the exception of the Semenoff model). Despite these minor quantitative differences, we find qualitatively the same phases in all models in similar ranges of n . We note that both chiral d wave and f wave result here in a fully gapped excitation spectrum. Fig. 3(a) shows the effective coupling strength for all models, which is roughly the same. We note that all models are particle-hole symmetric except Gr, and thus our results for the hole-doped case are the same as those shown in Fig. 3; here also for Gr the results do not change qualitatively for hole-doping³⁹. Panels (b)–(e) show the leading instabilities of each model individually. That is the key result of this Letter: we do not observe any relevant influence of the normal-state system’s topology onto the superconducting ground state for the considered models.

Increasing the gap size would lead to a much stronger contribution of the topological (trivial) term of the KM (Se and AF) model. Due to the \vec{k} dependence of the gap-opening term in the KM case, it is no longer possible to equalize the FSs. In fact, for a sufficiently large $t_2 > 0.2t_1$ (resulting in a gap as large as $2t_1$ ⁵⁷) for the KM model, we obtain an additional FS pocket which is

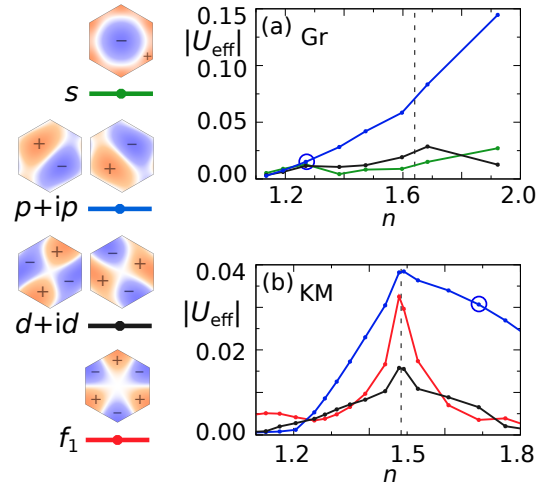


FIG. 4. Results for KM model with large gap ($t_2 = 0.5t_1$) and Gr model ($t_2 = 0.35t_1$) to feature a similar FS. The blue circles indicate where the Fermi surfaces in both shown models are still similar. The respective Fermi surfaces are shown in Fig. 2(b). Dashed lines indicate van Hove filling.

not the case for the Se and AF models, see Fig. 2(b). At least we are able to tune the Gr model such that it mimics the FS of the KM model. In analogy to the small gap case, we refer to it as the “large gap” case. Fig. 4 shows the results for Gr and KM models. Not unexpected, the superconducting phase diagrams are more diverse; they have, however, the common feature that the chiral p wave instability dominates (E_1 irrep). While the p wave instability for Gr is three-fold degenerate, due to the broken SU(2) symmetry the KM model only exhibits the two polarized triplet components $|\uparrow\uparrow\rangle$ and $|\downarrow\downarrow\rangle$ as leading instability. The blue circle indicates the point where the FSs are still similar [Fig. 2(b)], and indeed also the effective coupling U_{eff} is roughly the same. As before, the influence of the normal state’s topology seems to be irrelevant. We emphasize that both models have the common property that their FSs have pockets around the corners of the BZ in addition to the circular pocket centered around the Γ point. Our second key result is thus that large second neighbor hopping (real or imaginary), leading to additional Fermi surface pockets around the corners of the Brillouin zone in addition to the circular pocket around the center, seems to favor chiral p wave superconductivity. That is particularly exciting as the chiral p wave superconductor is known to host a Majorana zero mode at defects such as vortices or domain walls. Considering hole-doping instead, the KM results still remain unchanged; hole-doped Gr at $t_2 = 0.35$ features a chiral d wave state instead, due to the absence of the additional Fermi pockets at the corner of the Brillouin zone. Last but not least we emphasize that the Gr model has a drastically increased pairing potential U_{eff} [see Fig. 4(a)], implying that it realizes a TSC with a high critical temperature T_c ³⁹.

Our results were derived in the weak coupling regime,

and it remains unclear what might happen for larger U_0 and other interactions (some first steps were already taken⁵⁸). We note, however, that a doped Kane-Mele type model was studied recently for intermediate interaction strength $U_0 = 2.5 t_1$ ⁵⁹, also identifying chiral d wave as the leading instability due to a comparable Fermi surface with Fig. 2 a).

IV. CONCLUSION

We have investigated four different models on the honeycomb lattice: topological and trivial insulators as well as a variant of semi-metallic graphene. By carefully tuning the system parameters we have equalized the strong effect of the FS and of the energy bands, thus only retaining the normal state's topology as the difference between all considered models. We present rigorous results that there is *no* influence of the normal state's topology onto

the leading superconducting instability. Instead, we find for all considered models topologically non-trivial chiral d wave or odd-parity f wave superconductivity. Clearly hexagonal lattices are a promising place to search for TSCs. Our results further suggest that longer-ranged hoppings causing additional FS pockets to appear might be an interesting avenue to find topologically non-trivial p wave superconductivity.

ACKNOWLEDGMENTS

We acknowledge instructive discussions with R. Thomale and P. Brydon. SR acknowledges support from the Australian Research Council through Grants No. FT180100211 and No. DP200101118. KLH acknowledges the Deutsche Forschungsgemeinschaft (DFG), German Research Foundation, under Project No. 277974659. This research was undertaken using the HPC facility Spartan hosted at the University of Melbourne.

-
- ¹ M. Sato and Y. Ando, *Rep. Prog. Phys.* **80**, 076501 (2017).
 - ² D. A. Ivanov, *Phys. Rev. Lett.* **86**, 268 (2001).
 - ³ C. Nayak, S. H. Simon, A. Stern, M. Freedman, and S. Das Sarma, *Rev. Mod. Phys.* **80**, 1083 (2008).
 - ⁴ A. Ramires, D. F. Agterberg, and M. Sigrist, *Phys. Rev. B* **98**, 024501 (2018).
 - ⁵ M. Sato, *Phys. Rev. B* **79**, 214526 (2009).
 - ⁶ M. Sato, *Phys. Rev. B* **81**, 220504(R) (2010).
 - ⁷ L. Fu and E. Berg, *Phys. Rev. Lett.* **105**, 097001 (2010).
 - ⁸ M. Geier, P. W. Brouwer, and L. Trifunovic, *Phys. Rev. B* **101**, 245128 (2020).
 - ⁹ S. Ono, H. C. Po, and H. Watanabe, *Science Advances* **6**, eaaz8367 (2020).
 - ¹⁰ L. Fu and C. L. Kane, *Phys. Rev. Lett.* **100**, 096407 (2008).
 - ¹¹ R. M. Lutchyn, J. D. Sau, and S. Das Sarma, *Phys. Rev. Lett.* **105**, 077001 (2010).
 - ¹² Y. Oreg, G. Refael, and F. von Oppen, *Phys. Rev. Lett.* **105**, 177002 (2010).
 - ¹³ V. Mourik, K. Zuo, S. M. Frolov, S. R. Plissard, E. P. A. M. Bakkers, and L. P. Kouwenhoven, *Science* **336**, 1003 (2012).
 - ¹⁴ S. Nadj-Perge, I. K. Drozdov, J. Li, H. Chen, S. Jeon, J. Seo, A. H. MacDonald, B. A. Bernevig, and A. Yazdani, *Science* **346**, 602 (2014).
 - ¹⁵ A. Palacio-Morales, E. Mascot, S. Cocklin, H. Kim, S. Rachel, D. K. Morr, and R. Wiesendanger, *Science Advances* **5**, eaav6600 (2019).
 - ¹⁶ C. Kallin and J. Berlinsky, *Rep. Prog. Phys.* **79**, 054502 (2016).
 - ¹⁷ R. Nandkishore, L. S. Levitov, and A. V. Chubukov, *Nat. Phys.* **8**, 158 (2012).
 - ¹⁸ M. L. Kiesel, C. Platt, W. Hanke, D. A. Abanin, and R. Thomale, *Phys. Rev. B* **86**, 020507(R) (2012).
 - ¹⁹ W. Wu, M. M. Scherer, C. Honerkamp, and K. Le Hur, *Phys. Rev. B* **87**, 094521 (2013).
 - ²⁰ A. M. Black-Schaffer, W. Wu, and K. Le Hur, *Phys. Rev. B* **90**, 054521 (2014).
 - ²¹ A. M. Black-Schaffer and C. Honerkamp, *J. Phys. Condens. Matter* **26**, 423201 (2014).
 - ²² In non-centrosymmetric systems it is possible to avoid their annihilation by applying a small Zeeman field⁶⁰.
 - ²³ H. Tou, Y. Kitaoka, K. Asayama, N. Kimura, Y. Ōnuki, E. Yamamoto, and K. Maezawa, *Phys. Rev. Lett.* **77**, 1374 (1996).
 - ²⁴ E. Bauer, G. Hilscher, H. Michor, C. Paul, E. W. Scheidt, A. Griбанov, Y. Seropegin, H. Noël, M. Sigrist, and P. Rogl, *Phys. Rev. Lett.* **92**, 027003 (2004).
 - ²⁵ Y. Yanase and M. Sigrist, *J. Phys. Soc. Jap.* **77**, 124711 (2008).
 - ²⁶ Y. S. Hor, A. J. Williams, J. G. Checkelsky, P. Roushan, J. Seo, Q. Xu, H. W. Zandbergen, A. Yazdani, N. P. Ong, and R. J. Cava, *Phys. Rev. Lett.* **104**, 057001 (2010).
 - ²⁷ S. Sasaki, M. Kriener, K. Segawa, K. Yada, Y. Tanaka, M. Sato, and Y. Ando, *Phys. Rev. Lett.* **107**, 217001 (2011).
 - ²⁸ A. S. Erickson, J.-H. Chu, M. F. Toney, T. H. Geballe, and I. R. Fisher, *Phys. Rev. B* **79**, 024520 (2009).
 - ²⁹ M. Novak, S. Sasaki, M. Kriener, K. Segawa, and Y. Ando, *Phys. Rev. B* **88**, 140502(R) (2013).
 - ³⁰ S. Sasaki, Z. Ren, A. A. Taskin, K. Segawa, L. Fu, and Y. Ando, *Phys. Rev. Lett.* **109**, 217004 (2012).
 - ³¹ P. Zhang, K. Yaji, T. Hashimoto, Y. Ota, T. Kondo, K. Okazaki, Z. Wang, J. Wen, G. D. Gu, H. Ding, and S. Shin, *Science* **360**, 182 (2018).
 - ³² J. D. Rameau, N. Zaki, G. D. Gu, P. D. Johnson, and M. Weinert, *Phys. Rev. B* **99**, 205117 (2019).
 - ³³ Z. Wang, J. O. Rodriguez, L. Jiao, S. Howard, M. Graham, G. D. Gu, T. L. Hughes, D. K. Morr, and V. Madhavan, *Science* **367**, 104 (2020).
 - ³⁴ S. Ran, C. Eckberg, Q.-P. Ding, Y. Furukawa, T. Metz, S. R. Saha, I.-L. Liu, M. Zic, H. Kim, J. Paglione, and N. P. Butch, *Science* **365**, 684 (2019).
 - ³⁵ H. Zhang, C.-X. Liu, X.-L. Qi, X. Dai, Z. Fang, and S.-C. Zhang, *Nat. Phys.* **5**, 438 (2009).

- ³⁶ Y. Tanaka, Z. Ren, T. Sato, K. Nakayama, S. Souma, T. Takahashi, K. Segawa, and Y. Ando, *Nat. Phys.* **8**, 800 (2012).
- ³⁷ S. Raghu, S. A. Kivelson, and D. J. Scalapino, *Phys. Rev. B* **81**, 224505 (2010).
- ³⁸ S. Raghu, E. Berg, A. V. Chubukov, and S. A. Kivelson, *Phys. Rev. B* **85**, 024516 (2012).
- ³⁹ S. Wolf, T. L. Schmidt, and S. Rachel, *Phys. Rev. B* **98**, 174515 (2018).
- ⁴⁰ W. Cho, R. Thomale, S. Raghu, and S. A. Kivelson, *Phys. Rev. B* **88**, 064505 (2013).
- ⁴¹ C. Platt, W. Cho, R. H. McKenzie, R. Thomale, and S. Raghu, *Phys. Rev. B* **93**, 214515 (2016).
- ⁴² W. Cho, C. Platt, R. H. McKenzie, and S. Raghu, *Phys. Rev. B* **92**, 134514 (2015).
- ⁴³ T. Scaffidi, J. C. Romers, and S. H. Simon, *Phys. Rev. B* **89**, 220510(R) (2014).
- ⁴⁴ H. S. Røising, F. Flicker, T. Scaffidi, and S. H. Simon, *Phys. Rev. B* **98**, 224515 (2018).
- ⁴⁵ C. L. Kane and E. J. Mele, *Phys. Rev. Lett.* **95**, 146802 (2005).
- ⁴⁶ C. L. Kane and E. J. Mele, *Phys. Rev. Lett.* **95**, 226801 (2005).
- ⁴⁷ G. W. Semenoff, *Phys. Rev. Lett.* **53**, 2449 (1984).
- ⁴⁸ A. M. Black-Schaffer and K. Le Hur, *Phys. Rev. B* **92**, 140503(R) (2015).
- ⁴⁹ See Supplemental Material at [URL] for (i) symmetry considerations and further details of the models, (ii) technical aspects of the WCRG method, (iii) form factors of the superconducting instabilities and (iv) comparison of the bandstructures of the involved models.
- ⁵⁰ J. F. Annett, *Adv. Phys.* **39**, 83 (1990).
- ⁵¹ M. Altmeyer, D. Guterding, P. J. Hirschfeld, T. A. Maier, R. Valentí, and D. J. Scalapino, *Phys. Rev. B* **94**, 214515 (2016).
- ⁵² W. Metzner, M. Salmhofer, C. Honerkamp, V. Meden, and K. Schönhammer, *Rev. Mod. Phys.* **84**, 299 (2012).
- ⁵³ W. Kohn and J. M. Luttinger, *Phys. Rev. Lett.* **15**, 524 (1965).
- ⁵⁴ S. Wolf and S. Rachel, *Phys. Rev. B* **102**, 174512 (2020).
- ⁵⁵ O. Vafek and L. Wang, *Phys. Rev. B* **84**, 172501 (2011).
- ⁵⁶ R. Shankar, *Rev. Mod. Phys.* **66**, 129 (1994).
- ⁵⁷ S. Rachel and K. Le Hur, *Phys. Rev. B* **82**, 075106 (2010).
- ⁵⁸ K. Lee, T. Hazra, M. Randeria, and N. Trivedi, *Phys. Rev. B* **99**, 184514 (2019).
- ⁵⁹ X. Wu, M. Fink, W. Hanke, R. Thomale, and D. Di Sante, *Phys. Rev. B* **100**, 041117(R) (2019).
- ⁶⁰ M. Sato, Y. Takahashi, and S. Fujimoto, *Phys. Rev. B* **82**, 134521 (2010).

Topological superconductivity on the honeycomb lattice: Effect of normal state topology

Sebastian Wolf,¹ Tyler Gardener,¹ Karyn Le Hur,² and Stephan Rachel¹

¹*School of Physics, University of Melbourne, Parkville, VIC 3010, Australia*

²*CPHT, CNRS, Institut Polytechnique de Paris, Route de Saclay, 91128 Palaiseau, France*

I. SYMMETRY CONSIDERATIONS

Before we establish the specific Bloch matrices $\hat{h}(\vec{k})$ for all the models, we start with a symmetry analysis. The hexagonal model is given by two sublattice and two spin degrees of freedom, which in total yields a 4x4 Bloch matrix. This is in general given in the following form:

$$\hat{h}(\vec{k}) = \sigma_\nu \otimes \gamma^\nu(\vec{k}), \quad (\text{S1})$$

where the $\gamma^\nu(\vec{k})$ are 2x2 matrices, *i.e.*, they can be written as a sum of Pauli matrices τ_μ as well:

$$\gamma^\nu(\vec{k}) = \gamma_\mu^\nu(\vec{k}) \tau^\mu. \quad (\text{S2})$$

The symmetries of the system pose several constraints on $\gamma^\nu(\vec{k})$, which are obtained by

$$\hat{O} \hat{h} \hat{O}^\dagger = \hat{h}, \quad (\text{S3})$$

where \hat{O} is the operator of the symmetry operation. Explicit representations of relevant symmetries for the hexagonal lattice are listed in Tab. S1. It is more convenient to check the symmetries of γ_μ^ν than of γ^ν itself once we have more

TABLE S1. List of symmetry operators, $\hat{O} = \hat{O}_s \otimes \hat{O}_o \otimes \hat{O}_r$, for all symmetries in the D_6 group, time reversal, and inversion symmetries. \hat{O}_r denotes the part of \hat{O} which acts on real space, *i.e.*, on \vec{r} , \hat{O}_o the one which acts on orbital (sublattice) space, and \hat{O}_s the one which acts on spin space. Note that for time reversal, $\hat{T} = (\hat{T}_s \otimes \hat{T}_o \otimes \hat{T}_r)K$, where K denotes complex conjugation. $\mathbb{1}$ is the identity (given by σ_0 in spin space). Note that \hat{O}_r and \hat{O}_s are general, while \hat{O}_o depends on the specific arrangement of orbitals and sublattice sites in the crystal lattice.

Symmetry	\hat{O}_s	\hat{O}_o	\hat{O}_r
Time reversal	$-i\sigma_y$	τ_0	$\mathbb{1}$
Inversion	$i\sigma_0$	τ_x	$-\mathbb{1}$
C_2 rotation	$\pm i\sigma_z$	τ_x	$\begin{pmatrix} -1 & 0 & 0 \\ 0 & -1 & 0 \\ 0 & 0 & 1 \end{pmatrix}$
C_3 rotation	$\pm \left(\frac{1}{2}\sigma_0 + i\frac{\sqrt{3}}{2}\sigma_z \right)$	τ_0	$\begin{pmatrix} -1/2 & -\sqrt{3}/2 & 0 \\ \sqrt{3}/2 & -1/2 & 0 \\ 0 & 0 & 1 \end{pmatrix}$
C_6 rotation	$\pm \left(\frac{\sqrt{3}}{2}\sigma_0 + i\frac{1}{2}\sigma_z \right)$	τ_x	$\begin{pmatrix} 1/2 & -\sqrt{3}/2 & 0 \\ \sqrt{3}/2 & 1/2 & 0 \\ 0 & 0 & 1 \end{pmatrix}$
x reflection	$\pm\sigma_x$	τ_x	$\begin{pmatrix} -1 & 0 & 0 \\ 0 & 1 & 0 \\ 0 & 0 & 1 \end{pmatrix}$
y reflection	$\pm\sigma_y$	τ_0	$\begin{pmatrix} 1 & 0 & 0 \\ 0 & -1 & 0 \\ 0 & 0 & 1 \end{pmatrix}$

TABLE S2. List of constraints on γ^ν due to the symmetries listed in Tab. S1. The γ^ν are hermitian $N \times N$ matrices, where N is the number of orbitals per unit cell. Thus, they are real if $N = 1$. For $N > 1$ it is important to note that the complex conjugation of the time reversal operator also acts on γ . For the orbital degree of freedom in each symmetry operation, *i.e.*, the subscript μ in γ_μ^ν , we have either exchange of orbitals, τ_x , or the identity, τ_0 . Exchange means all γ_{yz}^ν gain an additional factor -1 .

Symmetry	Conditions for γ^ν	Conditions for γ_μ^ν
Time reversal	$\gamma^{0*}(-k) = \gamma^0(k)$, $(\gamma^{x,y,z})^*(-k) = -\gamma^{x,y,z}(k)$	Even: $\gamma_{0xz}^0, \gamma_y^{xyz}$ Odd: $\gamma_y^0, \gamma_{0xz}^{xyz}$
Inversion	$\tau_x \gamma^\nu(-k) \tau_x = \gamma^\nu(k)$	Even: $\gamma_0^\nu, \gamma_x^\nu$ Odd: $\gamma_y^\nu, \gamma_z^\nu$
C_2 rotation	$\tau_x \gamma^{0z}(-k) \tau_x = \gamma^{0z}(k)$ $\tau_x \gamma^{xy}(-k) \tau_x = -\gamma^{xy}(k)$	Even: $\gamma_{0x}^{0z}, \gamma_{yz}^{xy}$ Odd: $\gamma_{0x}^{xy}, \gamma_{yz}^{0z}$
C_3 rotation	$\gamma^{0z}(C_3 k) = \gamma^{0z}(k)$ $\gamma^x(C_3 k) = -\frac{1}{2}\gamma^x(k), \gamma^y(C_3 k) = -\frac{\sqrt{3}}{2}\gamma^y(k)$	Same for γ_μ^{0z} Same for $\gamma_\mu^x, \gamma_\mu^y$
C_6 rotation	$\gamma^{0z}(C_6 k) = \gamma^{0z}(k)$ $\gamma^x(C_6 k) = \frac{1}{2}\gamma^x(k), \gamma^y(C_6 k) = -\frac{\sqrt{3}}{2}\gamma^y(k)$	Even: γ_{0x}^{0z} , Odd: γ_{yz}^{0z} (under C_6) Same for $\gamma_{0x}^{x,y}$, factor -1 for $\gamma_{yz}^{x,y}$
x reflection	$\tau_x \gamma^{0x}(-k_x, k_y) \tau_x = \gamma^{0x}(k_x, k_y)$ $\tau_x \gamma^{yz}(-k_x, k_y) \tau_x = -\gamma^{yz}(k_x, k_y)$	Even in k_x : $\gamma_{0x}^{0x}, \gamma_{yz}^{yz}$ Odd in k_x : $\gamma_{0x}^{yz}, \gamma_{yz}^{x0}$
y reflection	$\gamma^{0y}(k_x, -k_y) = \gamma^{0y}(k_x, k_y)$ $\gamma^{xz}(k_x, -k_y) = -\gamma^{xz}(k_x, k_y)$	Even in k_y : γ_μ^{0y} Odd in k_y : γ_μ^{xz}

than one orbital per unit cell, since the Pauli matrices τ^ν complicate things. We have

$$\begin{pmatrix} \gamma^0 \\ \gamma^x \\ \gamma^y \\ \gamma^z \end{pmatrix} = \begin{pmatrix} \gamma_0^0 & \gamma_x^0 & \gamma_y^0 & \gamma_z^0 \\ \gamma_0^x & \gamma_x^x & \gamma_y^x & \gamma_z^x \\ \gamma_0^y & \gamma_x^y & \gamma_y^y & \gamma_z^y \\ \gamma_0^z & \gamma_x^z & \gamma_y^z & \gamma_z^z \end{pmatrix} \begin{pmatrix} \tau^0 \\ \tau^x \\ \tau^y \\ \tau^z \end{pmatrix}, \quad (\text{S4})$$

where we give conditions for the γ_μ^ν to conserve certain symmetries in Tab. S2. Thus, we can obtain the factor $D_{\mu\nu}$ in

$$\gamma_\mu^\nu(\hat{O}_r k) = D_{\mu\nu} \gamma_\mu^\nu(k) \quad (\text{S5})$$

arising from the given symmetry under the action of \hat{O}_r on k . Note that $D_{\mu\nu}$ is mostly just ± 1 , except for rotations which are not a multiple of $\pi/2$ and reflections that are not in x or y direction. In the following is a list of the factors $D_{\mu\nu}$ for several symmetries:

$$\begin{aligned} \text{Time reversal: } & \begin{pmatrix} + & + & - & + \\ - & - & + & - \\ - & - & + & - \\ - & - & + & - \end{pmatrix}, \quad \text{Inversion: } \begin{pmatrix} + & + & - & - \\ + & + & - & - \\ + & + & - & - \\ + & + & - & - \end{pmatrix}, \\ x \text{ reflection: } & \begin{pmatrix} + & + & - & - \\ + & + & - & - \\ - & - & + & + \\ - & - & + & + \end{pmatrix}, \quad y \text{ reflection: } \begin{pmatrix} + & + & + & + \\ - & - & - & - \\ + & + & + & + \\ - & - & - & - \end{pmatrix}, \\ C_2: & \begin{pmatrix} + & + & - & - \\ - & - & + & + \\ - & - & + & + \\ + & + & - & - \end{pmatrix}, \quad C_3: \begin{pmatrix} + & + & + & + \\ -\frac{1}{2} & -\frac{1}{2} & -\frac{1}{2} & -\frac{1}{2} \\ -\frac{\sqrt{3}}{2} & -\frac{\sqrt{3}}{2} & -\frac{\sqrt{3}}{2} & -\frac{\sqrt{3}}{2} \\ + & + & + & + \end{pmatrix}, \quad C_6: \begin{pmatrix} + & + & - & - \\ +\frac{1}{2} & +\frac{1}{2} & -\frac{1}{2} & -\frac{1}{2} \\ -\frac{\sqrt{3}}{2} & -\frac{\sqrt{3}}{2} & +\frac{\sqrt{3}}{2} & +\frac{\sqrt{3}}{2} \\ + & + & - & - \end{pmatrix}. \end{aligned} \quad (\text{S6})$$

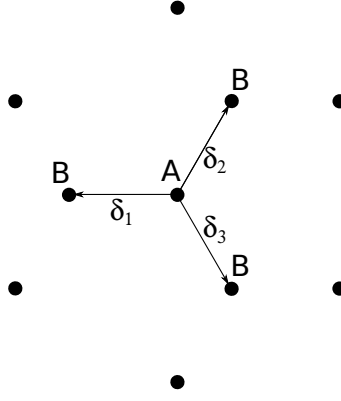


FIG. S1. Hexagonal lattice structure. Neighboring lattice sites are from different sublattices, A and B. The connecting vectors to the three nearest neighbors, δ_1 , δ_2 , and δ_3 , are shown.

II. HAMILTONIAN AND BLOCH MATRIX

The non-interacting tight-binding Hamiltonian is in general given by

$$H_0 = t_1 \sum_{\langle i,j \rangle} \sum_s c_{is}^\dagger c_{js} + t_2 \sum_{\langle i,j \rangle_2} \sum_s c_{is}^\dagger c_{js}. \quad (\text{S7})$$

The fundamental lattice structure of all models which will be considered here is that of graphene, which is shown in Fig. S1. We have two sites, A and B, per unit cell. The lattice consists of two triangular sublattices A and B, where the nearest neighbor to each lattice site is from the other sublattice. In the following, we will establish the Bloch matrix for each model. The crystal lattice and all hopping and onsite terms for each model are shown in Fig. 1 of the main text.

1. Graphene

For graphene (Gr), we consider nearest-neighbor hopping t_1 and second-neighbor hopping t_2 . The Bloch matrix of this system is given by

$$\hat{h}_{\text{Gr}} = \begin{pmatrix} T_3 & T_1 - iT_2 & 0 & 0 \\ T_1 + iT_2 & T_3 & 0 & 0 \\ 0 & 0 & T_3 & T_1 - iT_2 \\ 0 & 0 & T_1 + iT_2 & T_3 \end{pmatrix} \quad (\text{S8})$$

$$= \sigma_0 \otimes (T_3 \tau_0 + T_1 \tau_x + T_2 \tau_y), \quad (\text{S9})$$

$$T_1 = \text{Re}[t_1 \sum_i e^{k \cdot \delta_i}] = t_1 \left[\cos(k_x) + 2 \cos\left(\frac{1}{2}k_x\right) \cos\left(\frac{\sqrt{3}}{2}k_y\right) \right], \quad (\text{S10})$$

$$T_2 = -\text{Im}[t_1 \sum_i e^{k \cdot \delta_i}] = t_1 \left[\sin(k_x) - 2 \sin\left(\frac{1}{2}k_x\right) \cos\left(\frac{\sqrt{3}}{2}k_y\right) \right], \quad (\text{S11})$$

$$T_3 = -t_2 \left[2 \cos(\sqrt{3}k_y) + 4 \cos\left(\frac{\sqrt{3}}{2}k_y\right) \cos\left(\frac{3}{2}k_x\right) \right], \quad (\text{S12})$$

where we set the length $|\delta_i| = 1$. The functions T_1 , T_2 , and T_3 have the following parities:

$$T_1(k) = T_1(-k), \quad T_2(k) = -T_2(-k), \quad T_3(-k) = T_3(k). \quad (\text{S13})$$

The vector γ^ν is given by

$$\begin{pmatrix} \gamma^0 \\ \gamma^x \\ \gamma^y \\ \gamma^z \end{pmatrix} = \begin{pmatrix} T_3 & T_1 & T_2 & 0 \\ 0 & 0 & 0 & 0 \\ 0 & 0 & 0 & 0 \\ 0 & 0 & 0 & 0 \end{pmatrix} \begin{pmatrix} \tau^0 \\ \tau^x \\ \tau^y \\ \tau^z \end{pmatrix}. \quad (\text{S14})$$

This satisfies the conditions for all symmetries in Tab. S1.

2. Semenoff insulator

The Semenoff insulator¹ (Se) introduces a staggered sublattice potential, M , *i.e.*, we add a constant energy to the Hamiltonian which is positive on sublattice A and negative on sublattice B. This yields for the non-interacting Hamiltonian

$$H_0 = t_1 \sum_{\langle i,j \rangle} \sum_s c_{is}^\dagger c_{js} + M \sum_{i,s} (-1)^{\varepsilon_i} c_{is}^\dagger c_{is}, \quad (\text{S15})$$

$$\varepsilon_i = \begin{cases} 0 & \text{on sublattice A,} \\ 1 & \text{on sublattice B.} \end{cases} \quad (\text{S16})$$

The Bloch matrix takes the form

$$\hat{h}_{\text{Se}} = \begin{pmatrix} M & T_1 - iT_2 & 0 & 0 \\ T_1 + iT_2 & -M & 0 & 0 \\ 0 & 0 & M & T_1 - iT_2 \\ 0 & 0 & T_1 + iT_2 & -M \end{pmatrix} \quad (\text{S17})$$

$$= \sigma_0 \otimes (T_1 \tau_x + T_2 \tau_y + M \tau_z), \quad (\text{S18})$$

$$T_1 = \text{Re}[t_1 \sum_i e^{k \cdot \delta_i}] = t_1 \left[\cos(k_x) + 2 \cos\left(\frac{1}{2}k_x\right) \cos\left(\frac{\sqrt{3}}{2}k_y\right) \right], \quad (\text{S19})$$

$$T_2 = -\text{Im}[t_1 \sum_i e^{k \cdot \delta_i}] = t_1 \left[\sin(k_x) - 2 \sin\left(\frac{1}{2}k_x\right) \cos\left(\frac{\sqrt{3}}{2}k_y\right) \right]. \quad (\text{S20})$$

The functions T_1 , T_2 , and M have the following properties:

$$T_1(k) = T_1(-k), \quad T_2(k) = -T_2(-k), \quad M(k) = M(-k) = \text{const.} \quad (\text{S21})$$

The vector γ^ν is given by

$$\begin{pmatrix} \gamma^0 \\ \gamma^x \\ \gamma^y \\ \gamma^z \end{pmatrix} = \begin{pmatrix} 0 & T_1 & T_2 & M \\ 0 & 0 & 0 & 0 \\ 0 & 0 & 0 & 0 \\ 0 & 0 & 0 & 0 \end{pmatrix} \begin{pmatrix} \tau^0 \\ \tau^x \\ \tau^y \\ \tau^z \end{pmatrix}. \quad (\text{S22})$$

The term $\sigma_0 \otimes M \tau_z$ breaks inversion symmetry, since $M(k) = M(-k)$ (M is a constant) and thus $\tau_x M \tau_z \tau_x = -M \tau_z$. It also breaks every symmetry with $\hat{O}_o = \tau_x$, since the staggered potential breaks the symmetry between the sublattices A and B, namely C_2 , C_6 , and x reflection.

3. Antiferromagnetic order

A system with an additional antiferromagnetic Zeeman field (AF) yields the following Hamiltonian:

$$H_0 = t_1 \sum_{\langle i,j \rangle} \sum_s c_{is}^\dagger c_{js} + Z \sum_i \sum_{ss'} (-1)^{\varepsilon_i} c_{is}^\dagger s_{ss'}^z c_{is'}, \quad (\text{S23})$$

$$\varepsilon_i = \begin{cases} 0 & \text{on sublattice A,} \\ 1 & \text{on sublattice B.} \end{cases} \quad (\text{S24})$$

The resulting Bloch matrix is given by

$$\hat{h}_{\text{AF}} = \begin{pmatrix} Z & T_1 - iT_2 & 0 & 0 \\ T_1 + iT_2 & -Z & 0 & 0 \\ 0 & 0 & -Z & T_1 - iT_2 \\ 0 & 0 & T_1 + iT_2 & Z \end{pmatrix} \quad (\text{S25})$$

$$= \sigma_0 \otimes (T_1 \tau_x + T_2 \tau_y) + \sigma_z \otimes Z \tau_z, \quad (\text{S26})$$

$$T_1 = \text{Re}[t_1 \sum_i e^{k \cdot \delta_i}] = t_1 \left[\cos(k_x) + 2 \cos\left(\frac{1}{2}k_x\right) \cos\left(\frac{\sqrt{3}}{2}k_y\right) \right], \quad (\text{S27})$$

$$T_2 = -\text{Im}[t_1 \sum_i e^{k \cdot \delta_i}] = t_1 \left[\sin(k_x) - 2 \sin\left(\frac{1}{2}k_x\right) \cos\left(\frac{\sqrt{3}}{2}k_y\right) \right]. \quad (\text{S28})$$

The functions T_1 and T_2 have the following properties:

$$T_1(-k) = T_1(k), \quad T_2(-k) = -T_2(k), \quad Z(-k) = Z(k) = \text{const.} \quad (\text{S29})$$

The vector γ^ν is given by

$$\begin{pmatrix} \gamma^0 \\ \gamma^x \\ \gamma^y \\ \gamma^z \end{pmatrix} = \begin{pmatrix} 0 & T_1 & T_2 & 0 \\ 0 & 0 & 0 & 0 \\ 0 & 0 & 0 & 0 \\ 0 & 0 & 0 & Z \end{pmatrix} \begin{pmatrix} \tau^0 \\ \tau^x \\ \tau^y \\ \tau^z \end{pmatrix}. \quad (\text{S30})$$

The term $\sigma_z \otimes Z \tau_z$ breaks time reversal symmetry, inversion symmetry, and every symmetry with $\hat{O}_o = \tau_x$, which are C_2 , C_6 , and x reflection.

4. Kane-Mele model

The Kane-Mele model (KM) presents the quantum spin hall effect in a time reversal invariant system^{2,3}. The Hamiltonian reads

$$H_0 = t_1 \sum_{\langle i,j \rangle} \sum_s c_{is}^\dagger c_{js} + it_2 \sum_{\langle\langle i,j \rangle\rangle} \sum_{ss'} \nu_{ij} c_{is}^\dagger \tau_{ss'}^z c_{js'}, \quad (\text{S31})$$

$$\nu_{ij} = \begin{cases} -1 & \text{clockwise,} \\ +1 & \text{counter clockwise.} \end{cases} \quad (\text{S32})$$

The resulting Bloch matrix is given by

$$\hat{h}_{\text{KM}} = \begin{pmatrix} \Omega & T_1 - iT_2 & 0 & 0 \\ T_1 + iT_2 & -\Omega & 0 & 0 \\ 0 & 0 & -\Omega & T_1 - iT_2 \\ 0 & 0 & T_1 + iT_2 & \Omega \end{pmatrix} \quad (\text{S33})$$

$$= \sigma_0 \otimes (T_1 \tau_x + T_2 \tau_y) + \sigma_z \otimes \Omega \tau_z, \quad (\text{S34})$$

$$T_1 = \text{Re}[t_1 \sum_i e^{k \cdot \delta_i}] = t_1 \left[\cos(k_x) + 2 \cos\left(\frac{1}{2}k_x\right) \cos\left(\frac{\sqrt{3}}{2}k_y\right) \right], \quad (\text{S35})$$

$$T_2 = -\text{Im}[t_1 \sum_i e^{k \cdot \delta_i}] = t_1 \left[\sin(k_x) - 2 \sin\left(\frac{1}{2}k_x\right) \cos\left(\frac{\sqrt{3}}{2}k_y\right) \right], \quad (\text{S36})$$

$$\Omega = 2t_2 \left[2 \cos\left(\frac{3}{2}k_x\right) \sin\left(\frac{\sqrt{3}}{2}k_y\right) - \sin(\sqrt{3}k_y) \right]. \quad (\text{S37})$$

The functions T_1 , T_2 , and Ω have the following parities:

$$T_1(-k) = T_1(k), \quad T_2(-k) = -T_2(k), \quad \Omega(-k) = -\Omega(k). \quad (\text{S38})$$

The vector γ^ν is given by

$$\begin{pmatrix} \gamma^0 \\ \gamma^x \\ \gamma^y \\ \gamma^z \end{pmatrix} = \begin{pmatrix} 0 & T_1 & T_2 & 0 \\ 0 & 0 & 0 & 0 \\ 0 & 0 & 0 & 0 \\ 0 & 0 & 0 & \Omega \end{pmatrix} \begin{pmatrix} \tau^0 \\ \tau^x \\ \tau^y \\ \tau^z \end{pmatrix}. \quad (\text{S39})$$

This conserves all symmetries given in Tab. S1.

5. Summary

Summarizing, all symmetries of the four considered models are given in Tab. I of the main text.

III. BANDSTRUCTURE AND EIGENVECTORS

The full energy spectrum, $\xi(\vec{k})$, of the non-interacting system is obtained by diagonalizing \hat{h} via a unitary transformation,

$$\xi(\vec{k}) = \hat{U}^\dagger(\vec{k}) \hat{h}(\vec{k}) \hat{U}(\vec{k}) \quad (\text{S40})$$

$$= \begin{pmatrix} E(\vec{k}, -) & 0 & 0 & 0 \\ 0 & E(\vec{k}, -) & 0 & 0 \\ 0 & 0 & E(\vec{k}, +) & 0 \\ 0 & 0 & 0 & E(\vec{k}, +) \end{pmatrix}, \quad (\text{S41})$$

with the band index $n = \pm 1$. Note that all four systems preserve spin degeneracy, and therefore the energy does not depend on the pseudo-spin quantum number \tilde{s} . In other words, $E(\vec{k}, n, \tilde{s}) \equiv E(\vec{k}, n)$. The energy spectra for the four models are given by

$$E(\vec{k}, n) = \Lambda_0(\vec{k}) + n \sqrt{T_1^2(\vec{k}) + T_2^2(\vec{k}) + \Lambda_1^2(\vec{k})},$$

where $T_1(\vec{k})$ and $T_2(\vec{k})$ are given by the nearest-neighbor hopping, and $\Lambda_0(\vec{k})$ and $\Lambda_1(\vec{k})$ are model dependent and are given by

$$\text{Gr : } \Lambda_0(\vec{k}) = T_3(\vec{k}) = -t_2 \left[2 \cos(\sqrt{3}k_y) + 4 \cos\left(\frac{\sqrt{3}}{2}k_y\right) \cos\left(\frac{3}{2}k_x\right) \right], \quad \Lambda_1(\vec{k}) = 0, \quad (\text{S42})$$

$$\text{Se : } \Lambda_0(\vec{k}) = 0, \quad \Lambda_1(\vec{k}) = M = \text{const}, \quad (\text{S43})$$

$$\text{AF : } \Lambda_0(\vec{k}) = 0, \quad \Lambda_1(\vec{k}) = Z = \text{const}, \quad (\text{S44})$$

$$\text{KM : } \Lambda_0(\vec{k}) = 0, \quad \Lambda_1(\vec{k}) = \Omega(\vec{k}) = 2t_2 \left[2 \cos\left(\frac{3}{2}k_x\right) \sin\left(\frac{\sqrt{3}}{2}k_y\right) - \sin(\sqrt{3}k_y) \right]. \quad (\text{S45})$$

The corresponding eigenvectors of $\hat{h}(\vec{k})$, which make up the columns in $\hat{U}(\vec{k})$, are given in Tab. S3, where

$$e^{i\phi} = \frac{T_1(\vec{k}) + iT_2(\vec{k})}{\sqrt{T_1^2(\vec{k}) + T_2^2(\vec{k})}}, \quad \theta_n^x = \sqrt{1 + x/E(\vec{k}, n)}. \quad (\text{S46})$$

IV. WEAK COUPLING RG

To find the leading superconducting instabilities for the models outlined above, we use the WCRG method. This method has been discussed previously for spin-invariant systems and systems with lifted spin degeneracy⁴⁻⁷. Instead of a full derivation, we will just give a brief summary while pointing out the relevant differences.

In the following, we use the short notation for momentum, band index, and pseudo spin,

$$1 \equiv \vec{k}_1, n_1, \tilde{s}_1, \quad \bar{1} \equiv -\vec{k}_1, n_1, \tilde{s}_1, \quad 1' \equiv \vec{k}_1, n_1, \tilde{s}'_1. \quad (\text{S47})$$

The important quantity for calculating the superconducting instabilities in the WCRG method is the two-particle vertex Γ in the Cooper channel. Since the method explicitly demands weak coupling, we expand Γ in orders of the local electron-electron interaction, U_0 , up to second order,

$$\Gamma(2\bar{2}'\bar{1}'1) = \sum_{n=1}^{\infty} U_0^n \Gamma^{(n)}(2\bar{2}'\bar{1}'1) = U_0 \Gamma^{(1)}(2\bar{2}'\bar{1}'1) + U_0^2 \Gamma^{(2)}(2\bar{2}'\bar{1}'1) + \dots \quad (\text{S48})$$

The first order, $\Gamma^{(1)}$, is given by⁸

$$\Gamma^{(1)}(2\bar{2}'\bar{1}'1) = M(2\bar{2}'\bar{1}'1), \quad (\text{S49})$$

where the function M reads

$$M(4321) = \sum_{l,s \neq s'} v_{l,s}^*(4) v_{l,s}(1) v_{l,s'}^*(3) v_{l,s'}(2) - \sum_{l,s \neq s'} v_{l,s}^*(4) v_{l,s}(2) v_{l,s'}^*(3) v_{l,s'}(1). \quad (\text{S50})$$

Note that the first order just suppresses the plain s -wave solution due to the repulsive interaction, U_0 . The second order, $\Gamma^{(2)}$, splits into three topologically distinct parts^{8,9},

$$\Gamma^{(2)} = \frac{1}{2} \Gamma_{\text{BCS}} + \Gamma_{\text{ZS}} + \Gamma_{\text{ZS}'} . \quad (\text{S51})$$

The first contribution is referred to as the BCS diagram and the other two contributions to zero sound (ZS) diagrams⁹. The BCS diagram diverges logarithmically, which indicates a phase transition, *i.e.*, that the normal state becomes instable towards the superconducting state (superconductivity is the only instability in the weak coupling regime,¹⁰). The divergency is treated by renormalization, upon which we obtain the superconducting order parameter from the eigenvalue problem

$$\sum_{\hat{k}_1 n_1 \tilde{s}_1 \tilde{s}'_1} g(2\bar{2}'\bar{1}'1) \psi_i(\hat{k}_1 n_1 \tilde{s}_1 \tilde{s}'_1) = \lambda_i \psi_i(\hat{k}_2 n_2 \tilde{s}_2 \tilde{s}'_2), \quad (\text{S52})$$

where \hat{k} denote momenta on the Fermi surface, λ_i are the eigenvalues, and ψ_i the corresponding form factors projected onto the Fermi surface. The scaled vertex g is used instead of Γ since its eigenvalues renormalize independently, *i.e.*,

TABLE S3. Eigenvectors of the Bloch matrix for the four models.

Model	Gr	Se	AF	KM
$v^{n\downarrow}$	$\frac{1}{\sqrt{2}} \begin{pmatrix} 0 \\ 0 \\ 1 \\ ne^{i\phi} \end{pmatrix}$	$\frac{1}{\sqrt{2}} \begin{pmatrix} 0 \\ 0 \\ \theta_n^M \\ ne^{i\phi} \theta_{-n}^M \end{pmatrix}$	$\frac{1}{\sqrt{2}} \begin{pmatrix} 0 \\ 0 \\ \theta_{-n}^Z \\ ne^{i\phi} \theta_n^Z \end{pmatrix}$	$\frac{1}{\sqrt{2}} \begin{pmatrix} 0 \\ 0 \\ \theta_n^\Omega \\ ne^{i\phi} \theta_n^\Omega \end{pmatrix}$
$v^{n\uparrow}$	$\frac{1}{\sqrt{2}} \begin{pmatrix} 1 \\ ne^{i\phi} \\ 0 \\ 0 \end{pmatrix}$	$\frac{1}{\sqrt{2}} \begin{pmatrix} \theta_n^M \\ ne^{i\phi} \theta_{-n}^M \\ 0 \\ 0 \end{pmatrix}$	$\frac{1}{\sqrt{2}} \begin{pmatrix} \theta_n^Z \\ ne^{i\phi} \theta_{-n}^Z \\ 0 \\ 0 \end{pmatrix}$	$\frac{1}{\sqrt{2}} \begin{pmatrix} \theta_n^\Omega \\ ne^{i\phi} \theta_{-n}^\Omega \\ 0 \\ 0 \end{pmatrix}$

the most negative eigenvalue λ_{\min} of g is the leading superconducting instability. A relative measure for the critical temperature is given by

$$T_c \propto e^{-1/|\lambda_{\min}|} = e^{-1/\rho|U_{\text{eff}}|} . \quad (\text{S53})$$

The scaled vertex g is obtained from Γ by

$$\begin{aligned} g(2\bar{2}'\bar{1}'1) &= \tau(2) [\Gamma_{\text{ZS}}(2\bar{2}'\bar{1}'1) + \Gamma_{\text{ZS}'}(2\bar{2}'\bar{1}'1)] \tau(1) \\ &= \tau(2) [\Gamma_{\text{ZS}}(2\bar{2}'\bar{1}'1) - \Gamma_{\text{ZS}}(\bar{2}'2\bar{1}'1)] \tau(1) , \end{aligned} \quad (\text{S54})$$

where the scaling function $\tau(1)$ is defined for a discretized Fermi surface as

$$\tau(\hat{k}, n) = \sqrt{\rho_n \frac{l(\hat{k}, n) \bar{v}(n)}{S_F(n) v(\hat{k}, n)}} , \quad \frac{1}{\bar{v}(n)} = \sum_{\hat{k}} \frac{l(\hat{k}, n)}{S_F(n)} \frac{1}{v(\hat{k}, n)} . \quad (\text{S55})$$

Here, ρ_n denotes the density of states at the Fermi level of band n , $l(\hat{k}, n)$ the distance to the neighboring Fermi surface discretization points, $S_F(n)$ the total length of the Fermi surface of band n , and $v(\hat{k}, n)$ the Fermi velocity of band n at the momentum \hat{k} .

With the vertex Γ_{ZS} given by

$$\Gamma_{\text{ZS}}(2\bar{2}'\bar{1}'1) = \sum_{\vec{k}_3} \sum_{n_3 n_4} \sum_{\tilde{s}_3 \tilde{s}_4} M(\bar{2}'431) M(234\bar{1}') \frac{f(E(3)) - f(E(4))}{E(3) - E(4)} = -\Gamma_{\text{ZS}'}(\bar{2}'2\bar{1}'1) , \quad (\text{S56})$$

where $f(E)$ is the Fermi distribution, we obtain for the scaled vertex

$$g(\hat{k}_2 n_2 \tilde{s}_2 \tilde{s}'_2, \hat{k}_1 n_1 \tilde{s}_1 \tilde{s}'_1) = \tau(\hat{k}_2, n_2) \left[\Pi(\hat{k}_2 n_2 \tilde{s}_2 \tilde{s}'_2, \hat{k}_1 n_1 \tilde{s}_1 \tilde{s}'_1) - \Pi(-\hat{k}_2 n_2 \tilde{s}_2 \tilde{s}'_2, \hat{k}_1 n_1 \tilde{s}_1 \tilde{s}'_1) \right] , \quad (\text{S57})$$

$$\begin{aligned} \Pi(\hat{k}_2 n_2 \tilde{s}_2 \tilde{s}'_2, \hat{k}_1 n_1 \tilde{s}_1 \tilde{s}'_1) &= \sum_{\nu, \nu'} \sum_{\tilde{\zeta}, \tilde{\zeta}'} \int_{\text{BZ}} \frac{d^2 q}{(2\pi)^2} \frac{f(E(\vec{q}, \nu)) - f(E(\vec{Q}, \nu'))}{E(\vec{q}, \nu) - E(\vec{Q}, \nu')} \\ &\times M(-\hat{k}_2 n_2 \tilde{s}'_2, \vec{Q} \nu' \tilde{\zeta}', \vec{q} \nu \tilde{\zeta}, \hat{k}_1 n_1 \tilde{s}_1) M(\hat{k}_2 n_2 \tilde{s}_2, \vec{q} \nu \tilde{\zeta}, \vec{Q} \nu' \tilde{\zeta}', -\hat{k}_1 n_1 \tilde{s}'_1) , \end{aligned} \quad (\text{S58})$$

where $\vec{Q} = \vec{q} + \hat{k}_1 + \hat{k}_2$ and the integral runs over the whole Brillouin-zone (BZ). Since we have four different spin indices in g , there are 16 possible spin channels. However, due to hermiticity and fermionic anti-commutation relations, we are left with six independent spin channels, given by

$$A = g(\hat{k}_2 n_2 \tilde{\downarrow} \tilde{\downarrow}, \hat{k}_1 n_1 \tilde{\downarrow} \tilde{\downarrow}) , \quad (\text{S59})$$

$$B = g(\hat{k}_2 n_2 \tilde{\downarrow} \tilde{\downarrow}, \hat{k}_1 n_1 \tilde{\downarrow} \tilde{\uparrow}) = -g(-\hat{k}_2 n_2 \tilde{\downarrow} \tilde{\downarrow}, \hat{k}_1 n_1 \tilde{\uparrow} \tilde{\downarrow}) = g^*(\hat{k}_1 n_1 \tilde{\downarrow} \tilde{\uparrow}, \hat{k}_2 n_2 \tilde{\downarrow} \tilde{\downarrow}) = -g^*(-\hat{k}_1 n_1 \tilde{\uparrow} \tilde{\downarrow}, \hat{k}_2 n_2 \tilde{\downarrow} \tilde{\downarrow}) , \quad (\text{S60})$$

$$C = g(\hat{k}_2 n_2 \tilde{\downarrow} \tilde{\downarrow}, \hat{k}_1 n_1 \tilde{\uparrow} \tilde{\uparrow}) = g^*(\hat{k}_1 n_1 \tilde{\uparrow} \tilde{\uparrow}, \hat{k}_2 n_2 \tilde{\downarrow} \tilde{\downarrow}) , \quad (\text{S61})$$

$$D = g(\hat{k}_2 n_2 \tilde{\downarrow} \tilde{\uparrow}, \hat{k}_1 n_1 \tilde{\downarrow} \tilde{\uparrow}) = -g(-\hat{k}_2 n_2 \tilde{\downarrow} \tilde{\uparrow}, \hat{k}_1 n_1 \tilde{\uparrow} \tilde{\downarrow}) = -g(\hat{k}_2 n_2 \tilde{\downarrow} \tilde{\downarrow}, -\hat{k}_1 n_1 \tilde{\uparrow} \tilde{\uparrow}) = g(-\hat{k}_2 n_2 \tilde{\downarrow} \tilde{\downarrow}, -\hat{k}_1 n_1 \tilde{\uparrow} \tilde{\downarrow}) , \quad (\text{S62})$$

$$E = g(\hat{k}_2 n_2 \tilde{\downarrow} \tilde{\uparrow}, \hat{k}_1 n_1 \tilde{\uparrow} \tilde{\uparrow}) = -g(\hat{k}_2 n_2 \tilde{\uparrow} \tilde{\downarrow}, -\hat{k}_1 n_1 \tilde{\uparrow} \tilde{\uparrow}) = g^*(\hat{k}_1 n_1 \tilde{\uparrow} \tilde{\uparrow}, \hat{k}_2 n_2 \tilde{\downarrow} \tilde{\uparrow}) = g^*(\hat{k}_1 n_1 \tilde{\uparrow} \tilde{\uparrow}, -\hat{k}_2 n_2 \tilde{\uparrow} \tilde{\downarrow}) , \quad (\text{S63})$$

$$F = g(\hat{k}_2 n_2 \tilde{\uparrow} \tilde{\uparrow}, \hat{k}_1 n_1 \tilde{\uparrow} \tilde{\uparrow}) . \quad (\text{S64})$$

In all models studied here, since there are no spin-flips involved in the interaction, the spin channels B , C , and E vanish. This separates the channels with total pseudo-spin $\tilde{S} = \pm 1$ (A and F) from the channels with total pseudo-spin $\tilde{S} = 0$ (D).

The contribution of the eigenvectors to the vertex, as given by the functions $M(\dots)M(\dots)$ in Eq. (S58), can be

calculated analytically. The result is given by

$$\text{Gr: } \frac{1}{8} \left[1 + n_1 n_2 \nu \nu' \frac{T_r^4}{\sqrt{T_1^2(k_1) + T_2^2(k_1)} \sqrt{T_1^2(k_2) + T_2^2(k_2)} \sqrt{T_1^2(q) + T_2^2(q)} \sqrt{T_1^2(Q) + T_2^2(Q)}} \right], \quad (\text{S65})$$

$$\text{Se: } \frac{1}{8} \left[1 + \frac{T_r^4 + M^4}{E(k_1, n_1) E(k_2, n_2) E(q, \nu) E(Q, \nu')} + \frac{M^2}{E(Q, \nu') E(q, \nu)} + \frac{M^2}{E(k_1, n_1) E(Q, \nu')} \right. \\ \left. + \frac{M^2}{E(k_1, n_1) E(q, \nu)} + \frac{M^2}{E(k_2, n_2) E(Q, \nu')} + \frac{M^2}{E(k_2, n_2) E(q, \nu)} + \frac{M^2}{E(k_1, n_1) E(k_2, n_2)} \right], \quad (\text{S66})$$

$$\text{AF, } A \text{ and } F: \frac{1}{8} \left[1 + \frac{T_r^4 + Z^4}{E(k_1, n_1) E(k_2, n_2) E(q, \nu) E(Q, \nu')} + \frac{Z^2}{E(Q, \nu') E(q, \nu)} - \frac{Z^2}{E(k_1, n_1) E(Q, \nu')} \right. \\ \left. - \frac{Z^2}{E(k_1, n_1) E(q, \nu)} - \frac{Z^2}{E(k_2, n_2) E(Q, \nu')} - \frac{Z^2}{E(k_2, n_2) E(q, \nu)} + \frac{Z^2}{E(k_1, n_1) E(k_2, n_2)} \right], \quad (\text{S67})$$

$$\text{AF, } D: \frac{n_1 n_2}{8} \left[\frac{\sqrt{T_1^2(k_1) + T_2^2(k_1)} \sqrt{T_1^2(k_2) + T_2^2(k_2)}}{E(k_1, n_1) E(k_2, n_2)} \left(1 - \frac{Z^2}{E(q, \nu) E(Q, \nu')} \right) \right. \\ \left. + \frac{T_r^4 \left(1 - \frac{Z^2}{E(k_1, n_1) E(k_2, n_2)} \right) + i T_i^4 \left(\frac{Z}{E(k_1, n_1)} - \frac{Z}{E(k_2, n_2)} \right)}{\sqrt{T_1^2(k_1) + T_2^2(k_1)} \sqrt{T_1^2(k_2) + T_2^2(k_2)} E(q, \nu) E(Q, \nu')} \right], \quad (\text{S68})$$

$$\text{KM, } A \text{ and } F: \frac{n_1 n_2}{8} \left[\frac{\sqrt{T_1^2(k_1) + T_2^2(k_1)} \sqrt{T_1^2(k_2) + T_2^2(k_2)}}{E(k_1, n_1) E(k_2, n_2)} \left(1 + \frac{\Omega(q) \Omega(Q)}{E(q, \nu) E(Q, \nu')} \right) \right. \\ \left. + \frac{T_r^4 \left(1 - \frac{\Omega(k_1) \Omega(k_2)}{E(k_1, n_1) E(k_2, n_2)} \right) + i T_i^4 \left(\frac{\Omega(k_1)}{E(k_1, n_1)} - \frac{\Omega(k_2)}{E(k_2, n_2)} \right)}{\sqrt{T_1^2(k_1) + T_2^2(k_1)} \sqrt{T_1^2(k_2) + T_2^2(k_2)} E(q, \nu) E(Q, \nu')} \right], \quad (\text{S69})$$

$$\text{KM, } D: \frac{1}{8} \left[1 + \frac{T_r^4 - \Omega(k_1) \Omega(k_2) \Omega(q) \Omega(Q)}{E(k_1, n_1) E(k_2, n_2) E(q, \nu) E(Q, \nu')} + \frac{\Omega(Q) \Omega(k_2)}{E(Q, \nu') E(k_2, n_2)} + \frac{\Omega(Q) \Omega(k_1)}{E(Q, \nu') E(k_1, n_1)} \right. \\ \left. - \frac{\Omega(Q) \Omega(q)}{E(Q, \nu') E(q, \nu)} + \frac{\Omega(k_1) \Omega(k_2)}{E(k_1, n_1) E(k_2, n_2)} - \frac{\Omega(q) \Omega(k_2)}{E(q, \nu) E(k_2, n_2)} - \frac{\Omega(q) \Omega(k_1)}{E(q, \nu) E(k_1, n_1)} \right], \quad (\text{S70})$$

where

$$T_r^4 = [T_1(k_1) T_2(k_2) + T_1(k_2) T_2(k_1)] [T_1(q) T_2(Q) - T_2(q) T_1(Q)] \quad (\text{S71})$$

$$+ [T_1(k_1) T_1(k_2) - T_2(k_1) T_2(k_2)] [T_1(q) T_1(Q) + T_2(q) T_2(Q)], \\ T_i^4 = [T_1(k_1) T_2(k_2) + T_1(k_2) T_2(k_1)] [T_1(q) T_1(Q) + T_2(q) T_2(Q)] \quad (\text{S72}) \\ + [T_1(k_1) T_1(k_2) - T_2(k_1) T_2(k_2)] [T_2(q) T_1(Q) - T_1(q) T_2(Q)].$$

Note that the pseudo-spin indices disappeared. Their only effect is choosing the correct eigenvectors for each spin channel. In the expressions for the eigenvectors themselves, once the pseudo-spin is defined, the pseudo-spin indices do not appear. Furthermore, it is apparent that for AF and KM, the vertices with $\tilde{s}_z = 0$ are different from the ones with $S_z = \pm 1$, whereas in all other models there is not difference.

The parameters used for the calculations in the main paper for the small gap case are given in Tab. S4

V. FORM FACTORS OF THE SUPERCONDUCTING ORDER PARAMETER

Several examples of appearing formfactors will be given in the following.

Firstly, in the small gap case, the formfactors of the leading superconducting instability is the same for each of the five models, as discussed in the main text. A few examples of the formfactors projected to the FS are shown in Fig. S2. Panel (a) shows a node-less f -wave (irrep B_1) at $\mu = 0.8$. Increasing μ towards the van-Hove singularity, the gap is mostly concentrated around the points on the FS which are close to the M points in the Brillouin zone, where

the density of states diverges. This is shown in Fig. S2(b), where $\mu = 0.99$. Panel (c) shows one of the degenerate d -wave formfactors of the E_2 irrep, for $\mu = 1.1$. The high number of nodal lines indicates higher harmonics present in this state (cf. formfactor shown in the main text). At higher chemical potential, shown in panel (d) at $\mu = 1.4$, the formfactor becomes even more mixed with higher harmonics.

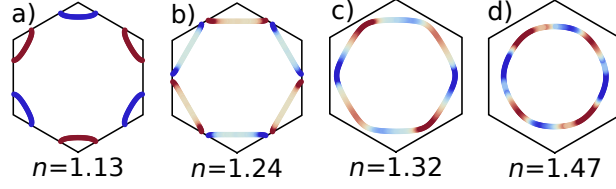


FIG. S2. Examples of formfactors in the small gap regime for several fillings n . The chemical potentials μ are (a) 0.8, (b) 0.99, (c) 1.1, and (d) 1.4. (a) and (b) show a node-less f -wave (irrep B_1), (c) and (d) a $d + id$ -wave (irrep E_2 , only one of the two degenerate d -waves is shown).

For the Kane-Mele model in the large gap case, *i.e.*, for $t_2 = 0.5$, the main text shows a dominating $p + ip$ -wave order parameter. Interestingly, this order parameter survives when the chemical potential μ is increased across the van-Hove singularity. The formfactors projected on the FS for values of μ between 1.85 and 2.5 are shown in Fig. S3, and show a very clean p -wave, *i.e.*, without contributions of higher harmonics.

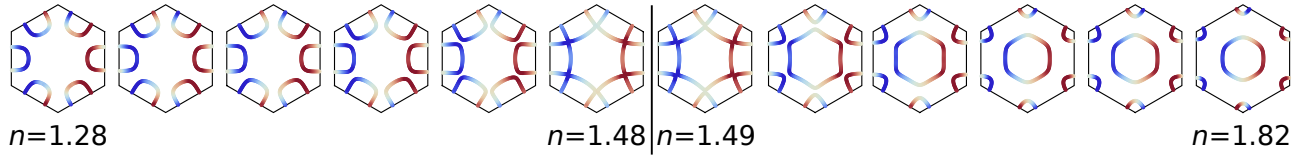


FIG. S3. Evolution of the p_x -wave formfactor in the Kane-Mele model for the large gap case for increasing filling n . The vertical line denotes the van-Hove singularity. Note that only the p_x -wave is shown, there is always a degenerate p_y -wave for each of the shown states.

For the graphene model, we show three formfactors in Fig. S4. Here, we show a nodeless extended s -wave in Fig. S4(a), and p -waves in (b) and (c).

TABLE S4. Parameter sets used for the calculations in the main text for the small gap case. Each line yields almost identical Fermi surfaces between the four models. For the large gap case, the graphene model has $t_2 = 0.35$ and the Kane-Mele model $t_2 = 0.5$ for all values of μ . For the fillings n marked with a star the following changes apply: at $n = 1.21$, the KM model has $n = 1.20$. At $n = 1.25$, the Gr model has $n = 1.255$. At $n = 1.28$, the Gr model has $n = 1.29$.

			Model	Gr	Se	AF	KM
Set	μ	n		t_2			
1	0.6	1.06		0.017	0.23	0.23	0.05
2	0.65	1.07		0.015	0.22	0.22	0.05
3	0.7	1.09		0.013	0.21	0.21	0.05
4	0.75	1.11		0.011	0.20	0.20	0.05
5	0.8	1.13		0.009	0.195	0.195	0.05
6	0.9	1.17		0.0055	0.15	0.15	0.05
7	0.95	1.21*		0.004	0.13	0.13	0.05
8	0.98	1.23		0.003	0.11	0.11	0.05
9	0.99	1.24		0.0025	0.11	0.11	0.05
10	1.01	1.25*		0.002	0.10	0.10	0.05
11	1.02	1.26		0.001	0.10	0.10	0.05
12	1.05	1.28*		0.003	0.11	0.11	0.05
13	1.1	1.32		0.004	0.12	0.12	0.05
14	1.2	1.37		0.004	0.13	0.13	0.05
15	1.4	1.47		0.004	0.13	0.13	0.05

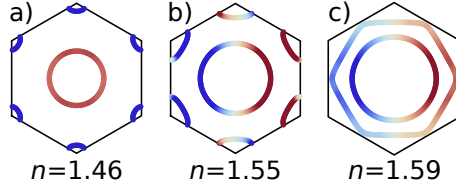


FIG. S4. Examples of the formfactors of the superconducting order parameter of graphene with second neighbor hopping $t_2 = 0.35$ for different fillings n . The shown formfactors are from leading superconducting instabilities. (a) shows a node-less extended s -wave at $\mu = 1.4$, (b) and (c) show one of the two degenerate p -wave states at $\mu = 1.6$ and $\mu = 1.71$, respectively.

VI. COMPARISON OF THE BANDSTRUCTURES

Here, we extend on our argument that eliminating the effect of the shape of the Fermi surface. In particular, we investigate the differences in the bandstructure between the models. This plays a role in the Lindhard function in Eq. (S58), *i.e.*, for the fraction

$$\frac{f(E(\vec{q}, \nu)) - f(E(\vec{Q}, \nu'))}{E(\vec{q}, \nu) - E(\vec{Q}, \nu')} . \quad (\text{S73})$$

Since we divide by the energy, momenta which are far away from the Fermi surface in terms of energy have negligible impact. In Fig. S5 we show the difference of the bandstructures between the KM, Se, and Gr models. Panel (a) shows the difference between KM and Se for the small gap case, panel (b) between KM and Gr in the small gap case, and panel (c) between KM and Gr in the large gap case. Overall, the KM and Se models are the most similar over the whole BZ, whereas for the comparison with Gr, we see the strongest deviations at the K and K' points. This is to be expected, since in the Gr model the gap closes at these points. In the large gap case, the bandstructures become more different, since the model-specific terms become larger. Around the Fermi surface, however, the difference is still small.

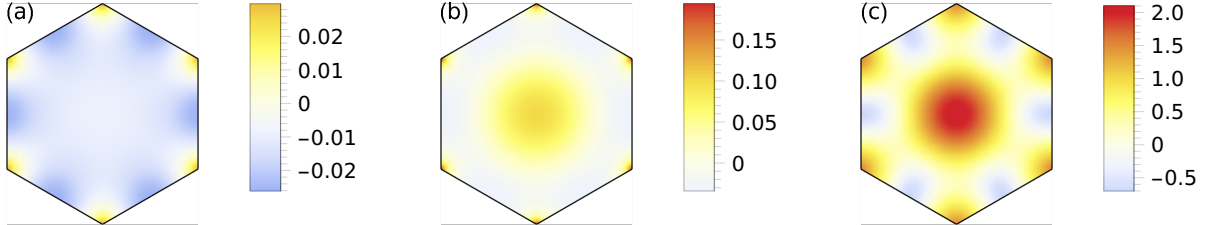


FIG. S5. Difference between the bandstructures of the models. We refer to the energy bands of the KM, Se and Gr models as E_{KM} , E_{Se} and E_{Gr} , respectively. (a) shows $E_{\text{KM}} - E_{\text{Se}}$ in the small gap case for $n = 1.06$ and $t_{2,\text{Se}} = 0.23$, (b) shows $E_{\text{KM}} - E_{\text{Gr}}$ in the small gap case for $n = 1.06$ and $t_{2,\text{Gr}} = 0.017$, and (c) shows $E_{\text{KM}} - E_{\text{Gr}}$ in the large gap case for $n_{\text{KM}} = 1$ and $n_{\text{Gr}} = 0.86$ ($\mu = 0$ in both cases).

-
- ¹ G. W. Semenoff, [Phys. Rev. Lett. **53**, 2449 \(1984\)](#).
² C. L. Kane and E. J. Mele, [Phys. Rev. Lett. **95**, 146802 \(2005\)](#).
³ C. L. Kane and E. J. Mele, [Phys. Rev. Lett. **95**, 226801 \(2005\)](#).
⁴ S. Raghu, S. A. Kivelson, and D. J. Scalapino, [Phys. Rev. B **81**, 224505 \(2010\)](#).
⁵ S. Raghu, E. Berg, A. V. Chubukov, and S. A. Kivelson, [Phys. Rev. B **85**, 024516 \(2012\)](#).
⁶ S. Wolf, T. L. Schmidt, and S. Rachel, [Phys. Rev. B **98**, 174515 \(2018\)](#).
⁷ S. Wolf and S. Rachel, [Phys. Rev. B **102**, 174512 \(2020\)](#).
⁸ O. Vafek and L. Wang, [Phys. Rev. B **84**, 172501 \(2011\)](#).
⁹ R. Shankar, [Rev. Mod. Phys. **66**, 129 \(1994\)](#).
¹⁰ W. Kohn and J. M. Luttinger, [Phys. Rev. Lett. **15**, 524 \(1965\)](#).